A DISCRETE DISLOCATION ANALYSIS OF NEAR-THRESHOLD FATIGUE CRACK GROWTH

V. S. DESHPANDE[1], A. NEEDLEMAN[1]† and E. VAN DER GIESSEN[2]

[1]Brown University, Division of Engineering, Providence, RI 02912, USA and [2]University of Groningen, Department of Applied Physics, Nyenborgh 4, 9747 AG Groningen, The Netherlands

Abstract—Analyses of cyclic loading of a plane strain mode I crack under small-scale yielding are carried out using discrete dislocation dynamics. The formulation is the same as used to analyze crack growth under monotonic loading conditions, differing only in the remote stress intensity factor being a cyclic function of time. The dislocations are all of edge character and are modeled as line singularities in an elastic solid. The lattice resistance to dislocation motion, dislocation nucleation, dislocation interaction with obstacles and dislocation annihilation are incorporated into the formulation through a set of constitutive rules. Either reversible or irreversible relations are specified between the opening traction and the displacement jump across a cohesive surface ahead of the initial crack tip in order to simulate cyclic loading as could occur in a vacuum or in an oxidizing environment, respectively. In accord with experimental data we find that the fatigue threshold ΔK_{th} is weakly dependent on the load ratio R when the reversible cohesive surface is employed. This intrinsic dependence of the threshold on R is an outcome of source limited plasticity at low R values and plastic shakedown at higher R values. On the other hand, ΔK_{th} is seen to decrease approximately linearly with increasing R followed by a plateau when the irreversible cohesive law is used. Our simulations show that in this case the fatigue threshold is dominated by crack closure at low values of R. Calculations illustrating the effects of obstacle density, tensile overloads and slip geometry on cyclic crack growth behavior are also presented. © 2001 Published by Elsevier Science Ltd on behalf of Acta Materialia Inc.

Keywords: Dislocations; Mechanical properties; Fatigue; Plastic; Computer simulation; Crack closure

1. INTRODUCTION

The essence of fatigue crack growth is that it occurs even when the driving force for crack growth is much smaller than what is needed for the same crack to grow under monotonic loading conditions. Amounts of crack growth less than an atomic spacing per loading cycle can lead to catastrophic failure over design lifetimes. Therefore, the conditions, if any, where crack growth under cyclic loading is precluded are of considerable interest. Operationally, this fatigue threshold is typically defined in terms of a maximum amount of crack growth per cycle, which is often taken as 10^{-8} mm per cycle [1]. Experimentally, the fatigue threshold is known to be sensitive to the material microstructure, the load history and the environment [1, 2].

Experiments to obtain the dependence of crack growth on these various parameters are difficult to carry out and time consuming because of the large number of cycles required for measurable amounts of crack growth to occur. Therefore, predictive models of the fatigue threshold have a potentially important role to play.

At the low driving force values in the near-threshold regime, plastic flow is confined to relatively small volumes. As a consequence, for crystalline metals, the discreteness of dislocations comes into play. The literature on dislocation models for fatigue crack growth has recently been reviewed by Riemelmoser *et al.* [3]. In particular, discrete dislocation models of threshold conditions for fatigue crack growth have been proposed by Pippan and co-workers [4–6] and Wilkinson *et al.* [7]. In these studies, dislocations nucleate from the crack tip (or from a single source near the crack tip). The dislocations then glide on specified slip planes emanating from the near crack tip region. Such models are meant to represent the deformation-controlled fatigue crack growth mechanism proposed by Laird and Smith [8] and Neumann [9]. By contrast, in our approach the material model is also applicable when there is no crack, see, for example, Ref. [10], and the fracture properties are

† To whom all correspondence should be addressed. Tel.: +1-404-863-2863; fax: +1-401-863-1157.

E-mail address: needle@engin.brown.edu (A. Needleman)

independent of whether the loading is monotonic or cyclic.

We analyze near-threshold fatigue crack growth in metal single crystals, where plastic flow arises from the collective motion of large numbers of dislocations. As in previous monotonic loading studies by Cleveringa *et al.* [11] and Van der Giessen *et al.* [12], full boundary value problem solutions are obtained for small-scale yielding of a mode I crack in plane strain. The loading is imposed by prescribing displacements corresponding to the isotropic, linear elastic mode I singular fields remote from the crack tip. The only difference from the problems in Refs [11, 12] is that the remote stress intensity factor is taken to be a cyclic function of time varying between a specified K_{min} and K_{max}. Plane strain conditions are taken to prevail and the dislocations, which are represented as line singularities in an elastic solid, are all of edge character. The planar model crystal has three slip systems, is initially free of mobile dislocations and the locations of dislocation sources and obstacles are specified in a process region surrounding the initial crack tip, with no special dislocation nucleation from the crack tip.

The solution of the boundary value problem for the dislocated solid follows the approach of Van der Giessen and Needleman [13] and Cleveringa *et al.* [10]. In this approach, the long range interactions between dislocations are accounted for through the continuum elasticity fields. Short range dislocation interactions are not represented by elasticity theory and are incorporated into the formulation through a set of constitutive rules, which are based on those proposed by Kubin *et al.* [14]. In particular, drag during dislocation motion, interactions with obstacles, and dislocation nucleation and annihilation are accounted for.

The fracture properties of the material are embedded in a cohesive surface constitutive relation [15], so that crack initiation and crack growth emerge as natural outcomes of the boundary value problem solution. A reversible cohesive constitutive relation is used to model conditions as could occur in a vacuum while an irreversible relation is used to represent an oxidizing environment. The cohesive surface model permits both normal and sliding modes of opening (although under the mode I conditions analyzed here only the opening mode is active) and crack growth is stress as well as deformation driven. In contrast, a solely deformation-controlled crack growth mechanism as used in Refs [4–7] does not account for the normal separation of the newly formed crack surface which gives rise to an open crack. Furthermore, cleavage is known to be a fatigue crack propagation mechanism, at least in intermetallics (e.g. Refs [16, 17]) and in nickel-based superalloys (e.g. Ref. [18]).

Cleveringa *et al.* [11] found the monotonic fracture behavior to depend sensitively on the interplay between the cohesive and plastic flow properties. For a sufficiently low density of dislocation sources, only

isolated dislocations are generated and crack propagation takes place in a brittle manner. On the other hand, when ample nucleation sites are available and the obstacle density is sufficiently low, the dislocations strongly relax the near-tip stresses, resulting in continued crack tip blunting without crack propagation. The circumstances to be considered in this paper fall between these two limiting situations so that decohesion accompanied by plastic dissipation takes place, as in Refs [16–18].

2. DISCRETE DISLOCATION FORMULATION

We consider an infinitely long crack in a two-dimensional single crystal subjected to far field mode I loading as sketched in Fig. 1a. Symmetry about the crack plane is assumed so that we need to consider only half of the crystal. This small-scale yielding problem is analyzed with plasticity assumed to be confined to a rectangular window of $L_p = 10$ μm by $h_p = 12.5$ μm inside of which dislocations are treated discretely; see Fig. 1a. The calculations are terminated before dislocations reach the boundary of this window. Remote from the crack tip, displacements corresponding to the isotropic, linear elastic mode I singular field are applied. With Cartesian coordinates x_i measured from the tip of the crack, the displacement components on the remote boundary are prescribed to be:

$$u_1 = \frac{K_I}{\mu}\sqrt{\frac{r}{2\pi}}\cos\frac{\theta}{2}\left(1-2\nu + \sin^2\frac{\theta}{2}\right) \qquad (1a)$$

$$u_2 = \frac{K_I}{\mu}\sqrt{\frac{r}{2\pi}}\sin\frac{\theta}{2}\left(2-2\nu-\cos^2\frac{\theta}{2}\right) \qquad (1b)$$

where

$$r = \sqrt{x_1^2 + x_2^2} \quad \theta = \tan^{-1}\left(\frac{x_2}{x_1}\right), \qquad (1c)$$

with μ the shear modulus, ν Poisson's ratio and K_I the mode I stress intensity factor.

Crack initiation and growth are modeled using a cohesive surface (see e.g. Ref. [19]) that extends over a distance of x_c in front of the initial crack. The properties of this cohesive surface will be specified later. Ahead of the cohesive surface, symmetry conditions are prescribed. The boundary value problem formulation and the numerical implementation follow that in Refs. [11, 12] where further details and additional references are given.

At each time step, an increment of the mode I stress intensity factor $\dot{K}_I\Delta t$ is prescribed. At the current instant, the stress and strain state of the body is
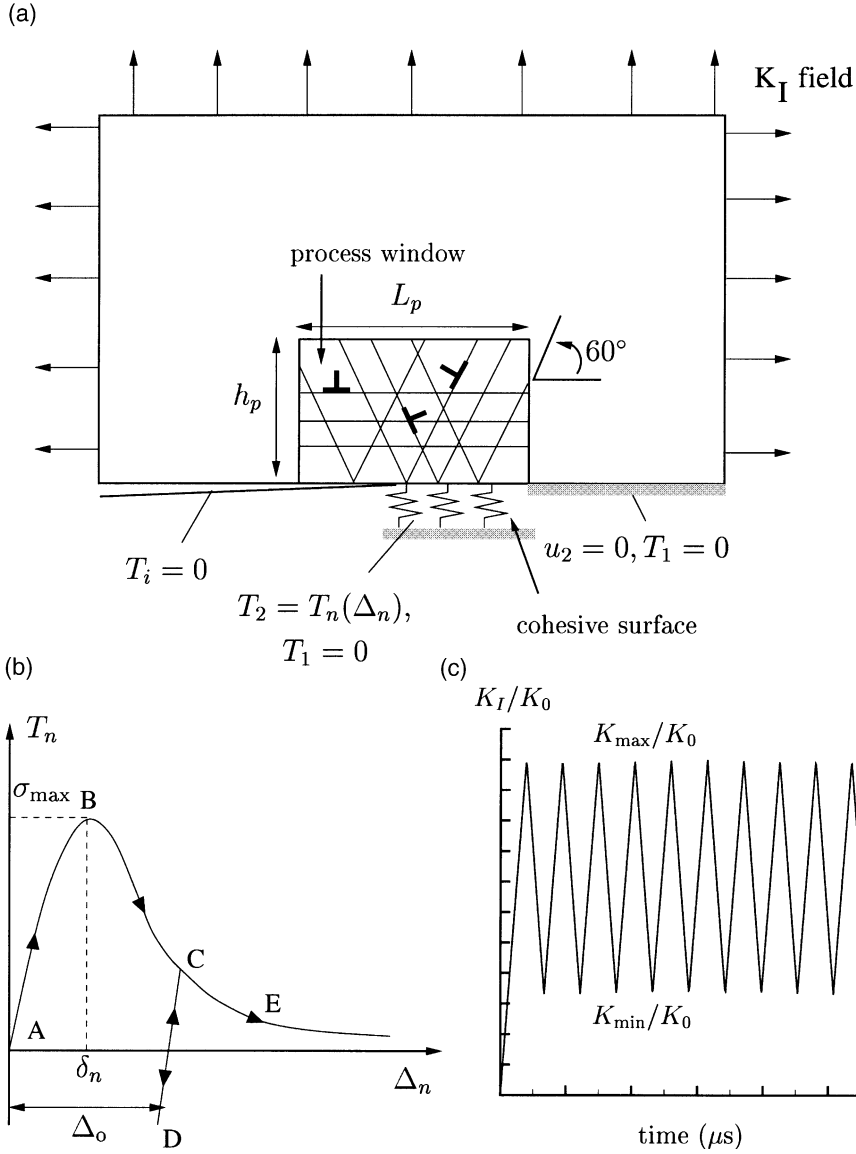
Fig. 1. (a) Mode I crack problem with the imposed boundary conditions. (b) Irreversible cohesive law. (c) Schematic of the applied stress intensity factor as a function of time.

known, so the forces on all dislocations can be calculated. On the basis of these forces we update the dislocation structure, which involves the motion of dislocations, the generation of new dislocations, their mutual annihilation, their pinning at obstacles, and their exit into the open crack. After this, the increments in the stress and strain fields are solved from the incremental version of the virtual work equation

$$\int_V \sigma_{ij}\delta\epsilon_{ij}\,\mathrm{d}V - \frac{1}{2}\int_{S_{\mathrm{coh}}} T_i\delta\Delta_i\,\mathrm{d}S = \int_{S_{\mathrm{ext}}} T_i\,\delta u_i\,\mathrm{d}S. \quad (2)$$

Here, V is the volume of the region analyzed, S_{ext} is

the external surface and S_{coh} is the surface across which cohesive tractions operate. Further, σ_{ij} are the components of the stress tensor, and

$$\epsilon_{ij} = \frac{1}{2}(u_{i,j} + u_{j,i}), \quad T_i = \sigma_{ij}v_j, \quad (3)$$

with v_i the components of the unit outward normal on S_{coh} or S_{ext}. The factor 1/2 in equation (2) stems from the fact that, by virtue of symmetry, only half of the work in the cohesive surface contributes to the work in the region analyzed.

Superposition is used to determine the velocity, strain-rate and stress-rate fields in the body with the new dislocation distribution [13]

$$\dot{u}_i = \tilde{\dot{u}} + \hat{\dot{u}}_i, \ \epsilon_{ij} = \tilde{\epsilon}_{ij} + \hat{\epsilon}_{ij}, \ \dot{\sigma}_{ij} = \tilde{\dot{\sigma}}_{ij} + \hat{\dot{\sigma}}_{ij}. \tag{4}$$

The (˜) fields are the sum of the fields of the individual dislocations, in their current configuration that give rise to tractions $\tilde{T}_i$ and displacements $\tilde{u}_i$ on the boundary of the body. The individual dislocation fields are those for an edge dislocation in a traction-free half-space [20], with the traction-free surface corresponding to the crack plane $x_2 = 0$. The (ˆ) fields represent the image fields that correct for the actual boundary conditions. Contrary to the (˜) fields, the latter are non-singular and are obtained with a finite element method.

With the decomposition (4), the Peach–Koehler force $f^{(k)}$ acting on the kth dislocation is given by

$$f^{(k)} = n_i^{(k)}(\hat{\sigma}_{ij} + \sum_{m \neq k} \sigma_{ij}^{(m)} + \Sigma_{ij}^{(k)})b_j^{(k)}. \tag{5}$$

Here, $n_i^{(k)}$ is the slip plane normal, $b_j^{(k)}$ is the Burgers vector and $\Sigma_{ij}^{(k)}$ is the image field on dislocation k due to the traction-free surface, that is, the difference between the half-space and infinite medium fields. The direction of the Peach–Koehler force is in the slip plane and normal to the dislocation line.

The elastic response of the material is taken to be isotropic, with shear modulus $\mu = 26.3$ GPa and Poisson's ratio $\nu = 0.33$. Plastic deformation is assumed to occur by the motion of edge dislocations only, with Burgers vector $b = 0.25$ nm. Dislocation motion is taken to occur by glide only with no cross slip so that dislocations remain on their slip planes. The magnitude of the glide velocity $v^{(k)}$ of dislocation k is prescribed to be linearly related to the Peach–Koehler force $f^{(k)}$ through the drag relation $f^{(k)} = Bv^{(k)}$, with $B = 10^{-4}$ Pa s, which is a representative value for aluminum [14].

Initially, the crystal is assumed to be free of mobile dislocations, but to contain a random distribution of dislocation sources and point obstacles. The sources mimic Frank–Read sources and generate a dislocation dipole when the magnitude of the Peach–Koehler force exceeds a critical value of $b\tau_{\mathrm{nuc}}$ during a period of time t_{nuc}, with $\tau_{\mathrm{nuc}} = 50$ MPa and $t_{\mathrm{nuc}} = 10$ ns. The obstacles, which could be small precipitates or forest dislocations, pin dislocations and release them once the Peach–Koehler force attains the obstacle strength $b\tau_{\mathrm{obs}}$, where $\tau_{\mathrm{obs}} = 150$ MPa. Annihilation of two dislocations with opposite Burgers vector occurs when they approach each other within a critical annihilation distance $L_{\mathrm{e}} = 6b$.

Both reversible and irreversible cohesive traction–displacement relations are employed to account for cyclic loading in non-oxidizing (vacuum) and oxidizing environments, respectively. We start by considering monotonic loading processes resulting in pure mode I opening of the crack. As the incipient fracture surface opens under the action of the loads, the opening is resisted by cohesion at the atomistic scale. We assume that the normal cohesive traction T_{n} has the universal binding form [21]

$$T_{\mathrm{n}}(\Delta_{\mathrm{n}}) = -\mathrm{e}\sigma_{\max}\frac{\Delta_{\mathrm{n}}}{\delta_{\mathrm{n}}}\exp\left(-\frac{\Delta_{\mathrm{n}}}{\delta_{\mathrm{n}}}\right), \tag{6}$$

where Δ_{n} is the total separation of the cohesive surface, $\Delta_{\mathrm{n}} = 2u_2(x_2 = 0)$, and T_{n} is the traction normal to the cohesive surface. As the cohesive surface separates, the magnitude of the traction increases, reaches a maximum and then approaches zero with increasing separation. To model conditions as could occur in a perfect vacuum where there is no oxidation of the newly formed surface, this relation is taken to be followed in a reversible manner. The other limiting case of complete oxidation of the newly formed surfaces, which is expected under normal atmospheric conditions, is modeled by an irreversible cohesive law. Partial oxidation of the newly formed surfaces is not treated here, but has been observed experimentally, as reported by Pelloux [22, 23] for Al alloys fatigued in a weak vacuum.

The effect of the formation of the oxide layer and the subsequent surface contact during unloading is modeled by specifying unloading from and reloading to the monotonic cohesive law according to the linear incremental relation

$$\dot{T}_{\mathrm{n}}(\Delta_{\mathrm{n}}) = -\frac{\mathrm{e}\sigma_{\max}}{\delta_{\mathrm{n}}}\dot{\Delta}_{\mathrm{n}}. \tag{7}$$

An example of a typical $T_{\mathrm{n}}-\Delta_{\mathrm{n}}$ path for the irreversible cohesive law is shown in Fig. 1b. The traction T_{n} increases with loading from A up to a maximum value at B followed by a softening response as per the universal binding law (6). The residual opening Δ_{o} marked in Fig. 1b represents the thickness of the oxide layer on the newly created surface. Unloading takes place along the path CD. Upon reloading, the traction increases along DC and then follows the universal binding law (6) along CE.

In de-Andrés *et al.* [24] and Nguyen *et al.* [25] irreversible cohesive surface descriptions were used in conjunction with conventional continuum plasticity to model fatigue crack growth. In Ref. [24] unloading occurs toward the origin, while in Ref. [25] the unloading–reloading hysteresis has the effect of reducing the cohesive strength as cyclic loading progresses. The irreversibility of the cohesive law used here gives rise to a residual opening but does not affect the cohesive strength.

The parameters used in this study are $\sigma_{\max} = 0.6$ GPa and $\delta_{\mathrm{n}} = 4b$ giving a work of separation, $\phi_{\mathrm{n}} = \mathrm{e}\sigma_{\max}\delta_{\mathrm{n}}$ of 1.63 J/m². The work of separation can be related to a reference stress intensity factor K_0 defined by

$$K_0 = \sqrt{\frac{E\phi_n}{1-v^2}}. \qquad (8)$$

For the material parameters used here $K_0 = 0.358$ MPa$\sqrt{m}$. The significance of K_0 is that crack growth in an elastic solid with the given cohesive properties takes place at $K_I/K_0 = 1$ [26]. For numerical reasons, the value of σ_{max} used here is about a factor of four smaller than the theoretical strength of aluminum. This small value of σ_{max} was used since the length scale over which large gradients occur in an elastic solid is proportional to the cohesive length $(E/\sigma_{max})\delta_n$ [27].

In all calculations, a finite element mesh of 120×100 bilinear quadrilateral elements was employed. Inside the process region, there is a graded 80×80 element mesh, with the minimum mesh spacing ≈ 0.01 μm. This can be compared with a cohesive length, $(E/\sigma_{max})\delta_n \approx 0.1$ μm. Resolving the dislocation dynamics requires a small time step of $\Delta t = 0.5$ ns. Thus, the calculations were carried out with a rather high loading rate of $\dot{K}_I = 100$ GPa$\sqrt{m}$/s in order to reduce the time required for the computations. The effect of loading rate is not explored here. However, in Ref. [28], under monotonic loading conditions, varying the loading rate by two orders of magnitude was not found to change the crack growth behavior qualitatively, although, of course, a strong tendency was found for increased plastic deformation at lower loading rates.

3. NUMERICAL RESULTS

In the calculations presented here the applied stress intensity factor K_I was varied with time between K_{min} and K_{max} as shown schematically in Fig. 1c. The ratio $R = K_{min}/K_{max}$ and the difference $\Delta K_I = K_{max} - K_{min}$ are used to characterize the cyclic loading. To determine the fatigue threshold, calculations were carried out with R fixed, starting at some ΔK_I and then reducing it until a cycle-by-cycle crack growth rate da/d$N \le 10^{-3}$ μm/cycle was obtained. The fatigue threshold, ΔK_{th}, was then defined to lie within the last two values of the applied ΔK_I. Typically steps of $\Delta K_I/K_0 = 0.05$ were used.

3.1. Reference case

We present cyclic loading results for a reference case using both the reversible and irreversible cohesive surface laws. The reference material has three slip systems such that the slip planes make angles $\phi^{(\alpha)} = (-60°, 0°, +60°)$ with the crack plane $x_2 = 0$. All slip planes have a spacing of $86b$ in the process window. The material is initially dislocation-free with a random source distribution having a density of $\rho_{src} = 60$/μm² and a random obstacle distribution having a density $\rho_{obs} = 290$/μm² (densities are per unit area in the process region). The source and obstacle distributions are shown in Fig. 2a; there is no special dislocation nucleation from the crack tip.

3.1.1. Fatigue with a reversible cohesive law.

For comparison purposes, a calculation was carried out with K_I monotonically increasing. The curve of K_I versus crack advance Δa is shown in Fig. 2b. Here and subsequently, the crack location is taken to be the point along the cohesive surface where $\Delta_n = 4\delta_n$. Crack growth initiates at $K_I/K_0 \approx 1.09$. This is followed by substantial plasticity and a sharp rise in the resistance to crack growth (Fig. 2b). Here, as seen by Cleveringa et al. [11], crack growth under monotonic loading occurs in "spurts" with the dislocations playing a dual role in the fracture process. On the one hand, local stress concentrations associated with discrete dislocations near the crack tip together with the stress concentration associated with the crack itself cause the crack to propagate. On the other hand, plasticity caused by the motion of the dislocations increases the resistance to crack growth and tends to arrest the crack.

Next consider cyclic loading with the stress intensity factor having a prescribed cyclic time dependence as shown schematically in Fig. 1c. Crack advance versus time curves for $R = 0.3$ and two values of ΔK_I are shown in Fig. 3a. In both cases K_{max} is higher than that required for crack growth to initiate under monotonic loading conditions so that a "burst" of crack growth occurs during the first loading cycle. Subsequently, for the case with $\Delta K_I/K_0 = 1.12$ the behavior settles down to an incremental crack growth da/d$N \approx 3 \times 10^{-3}$ μm/cycle while for $\Delta K_I/K_0 = 0.98$, da/d$N < 10^{-3}$ μm/cycle. Thus, $0.98 < \Delta K_{th}/K_0 < 1.12$. It is worth emphasizing here that we get continued crack growth under cyclic loading for a value of K_{max} at which the crack would have arrested under monotonic loading.

Figure 3b clearly shows that the dislocation density (per unit area in the process window) increases with the number of loading cycles for $\Delta K_I/K_0 = 1.12$. Consequently, the dislocation structures at the end and beginning of each cycle are not the same. This is demonstrated in Figs 4a and b showing the dislocation structure after the first and seventh load peak, respectively. For $\Delta K_I/K_0 = 0.98$, which is below the threshold, there is gradual increase in the dislocation density during the first eight cycles, shown in Fig. 3b, but this is followed by "plastic shakedown" with no cycle-by-cycle change in the dislocation density (not shown in Fig. 3b).

Similar cyclic loading calculations were carried out for various values of R. The results of those calculations are summarized in Fig. 5a, with the bars representing bounds on the computed value of ΔK_{th}. Figure 5a reveals that ΔK_{th} is insensitive to the load ratio for $R > 0.3$. Below this value of R the fatigue threshold increases with decreasing values of R.

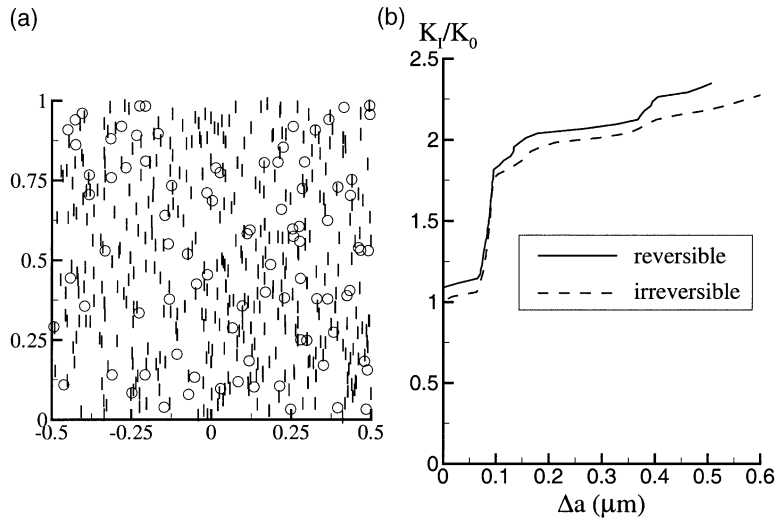The calculations indicate an intrinsic effect of the load ratio R on ΔK_{th} because no crack closure was

Fig. 2. (a) Dislocation source and obstacle distribution in a 1 μm×1 μm region around the initial crack tip for the reference material ($\rho_{src} = 60/\mu m^2$ and $\rho_{obs} = 290/\mu m^2$). The dislocation sources are represented by "o" and the obstacles by "|". (b) Applied stress intensity factor K_I/K_0 versus crack extension Δa for monotonic loading with the reversible and irreversible cohesive surface laws.
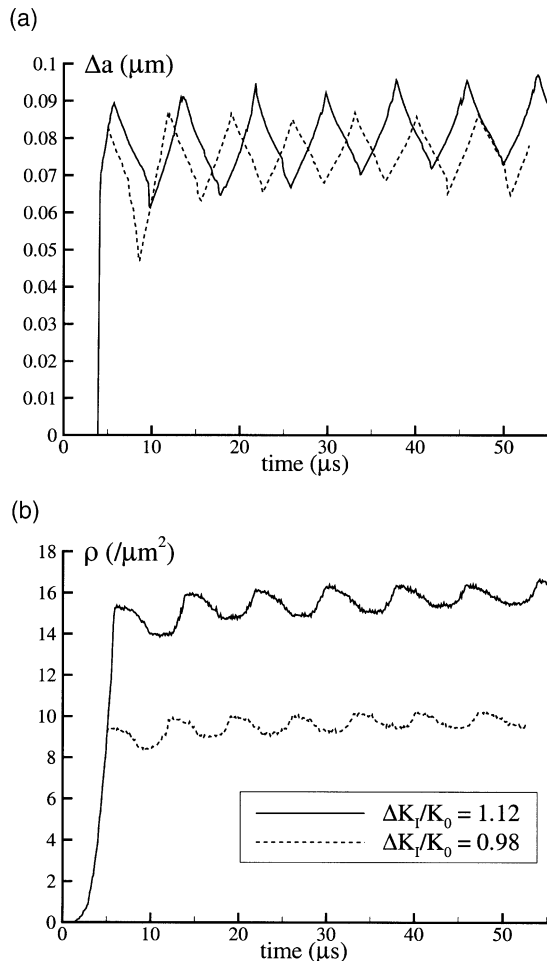

Fig. 3. (a) Time evolution of the crack growth and (b) time evolution of the dislocation density for the case with the reversible cohesive surface law ($R = 0.3$).

observed, even at $R = 0.1$. To understand the intrinsic dependence of the fatigue threshold on the load ratio R, the data are plotted in Fig. 5b using the axes ΔK_{th} and K_{max}. The figure suggests that crack growth can occur under cyclic loading if and only if: (i) the cyclic amplitude ΔK_I exceeds a critical value ΔK_{th}^*; and (ii) the maximum stress intensity K_{max} exceeds a critical value K_{max}^*.

The existence of these two parameters can be rationalized by first making the following general observations: with a reversible cohesive law, fatigue cannot occur if the material behavior is elastic because the state of the system then only depends on the current value of the loading parameter and not on its history. As a consequence, crack growth in an elastic system either occurs in the first cycle or it does not occur at all. In addition, if the state of the system does not change during the unloading–reloading part of the cycle, fatigue crack growth is also precluded because the response then only depends on the peak value and not on how (or when) it is attained. Hence,

1. For sufficiently low K_{max}, no dislocations are generated and the system is elastic. Therefore, for fatigue to occur with a reversible cohesive law, K_{max} must be at least large enough to nucleate dislocations in the surrounding field (this value depends on the source distribution). Effectively, there must be some minimum amount of plastic dissipation. Consequently, fatigue cannot occur below a minimum K_{max} denoted by K_{max}^*.

2. For $K_{max} \gg K_{max}^*$, interactions within the now dense dislocation structure act to retard dislocation motion. Accordingly, a minimum cyclic stress intensity factor range ΔK_I is needed to induce dislocation motion during unloading and reloading. Thus, in this regime, ΔK_I below a critical threshold value ΔK_{th}^* precludes crack growth.

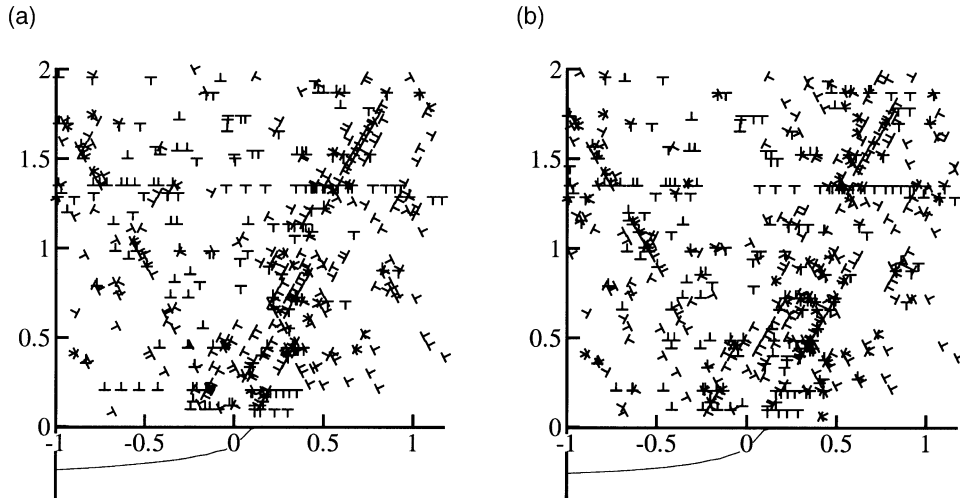(a)   (b)

Fig. 4. Dislocation structures for the case with the reversible cohesive law ($R = 0.3$ and $\Delta K_I/K_0 = 1.12$) at (a) the first and (b) the seventh load peak. All distances are in μm. The crack opening profiles (displacements magnified by a factor of 10) are plotted below the x_1-axis.

3.1.2. Fatigue with an irreversible cohesive law.

The monotonic K_I versus crack extension Δa curve for the irreversible cohesive law is shown in Fig. 2b. Compared to the calculation with the reversible cohesive surface, crack growth initiates slightly earlier at $K_I/K_0 \approx 1.03$. This difference arises from local unloading effects due to individual dislocations.

As with the reversible cohesive law, a series of calculations are carried out with a fixed value of R in which ΔK_I is decreased until a crack growth rate $da/dN < 10^{-3}$ μm/cycle is obtained. Results from a typical set of calculations with $R = 0.3$ and with three values of ΔK_I are shown in Fig. 6. In Fig. 6a, crack growth occurs during the first loading cycle for $\Delta K_I/K_0 = 0.77$, while crack advance does not commence until the third loading cycle for $\Delta K_I/K_0 = 0.707$ and until the fourth loading cycle for $\Delta K_I/K_0 = 0.658$. These results are consistent with the monotonic loading results of Fig. 2b where an initiation level of $1.03K_0$ was found. For the cases with $\Delta K_I/K_0 = 0.77$ and 0.707 we see that after the initial "burst" of crack growth, the behavior settles down to an incremental growth rate $da/dN \approx 6 \times 10^{-3}$ μm/cycle and 2×10^{-3} μm/cycle, respectively. This incremental crack advance takes place due to a "spurt" of crack growth towards the end of every loading cycle (see the inset in Fig. 6a). On the other hand, for $\Delta K_I/K_0 = 0.658$ the crack advances and retracts during every loading and unloading phase. Thus, for $R = 0.3$ we have $0.658 < \Delta K_{th}/K_0 < 0.707$.

The time evolution of the dislocation densities plotted in Fig. 6b shows that for $\Delta K_I/K_0 = 0.77$ and 0.707, the dislocation densities increase rapidly during the first few cycles corresponding to the high crack growth rates. Subsequently, the rate of increase of the dislocation density settles down and attains a value that is approximately the same for both

$\Delta K_I/K_0 = 0.77$ and 0.707. By contrast, after the first two cycles no cycle-by-cycle change in the dislocation density is seen in the case with $\Delta K_I/K_0 = 0.658$. Examination of the time evolution of the dislocation densities revealed that there is a rapid increase in the dislocation density corresponding to the "spurt" of crack growth near the end of every loading cycle (for $\Delta K_I/K_0 = 0.77$ and 0.707). This results in multiple slip systems becoming simultaneously active and gives rise to the crack length fluctuations seen towards the end of every loading cycle (inset of Fig. 6a).

Values of ΔK_{th} estimated from a series of calculations for different values of R are summarized in Fig. 5a. We see that ΔK_{th} decreases approximately linearly with increasing R up to $R_c \approx 0.6$, followed by a plateau. The results replotted in Fig. 5b using the axes of ΔK_{th} versus K_{max} look similar to those with the reversible cohesive law, albeit with smaller values of ΔK_{th}^* and $K_{max}^* = \Delta K_{th}^*/(1 - R_c)$. However, the mechanisms involved are quite different.

The unloading path specified in the irreversible cohesive law simulates surface contact due to the formation of oxide layers on the newly created surfaces: locations along the cohesive surface where the opening Δ_n exceeds $4\delta_n$ but are under the action of compressive surface tractions correspond to points where closure has occurred. Closure in our simulations occurred in the following manner. On unloading from the maximum load, the surfaces at the original location of the crack tip ($x_1 = 0$) first come into contact. Further reduction in the applied K_I results in this contact zone spreading from the original crack tip towards the current crack tip, as shown schematically in Fig. 7. Complete closure with contact of the crack faces at the current location of the crack tip occurs at an applied stress intensity factor $K_I = K_{cl}$. Upon reloading, the crack faces first separate at the current
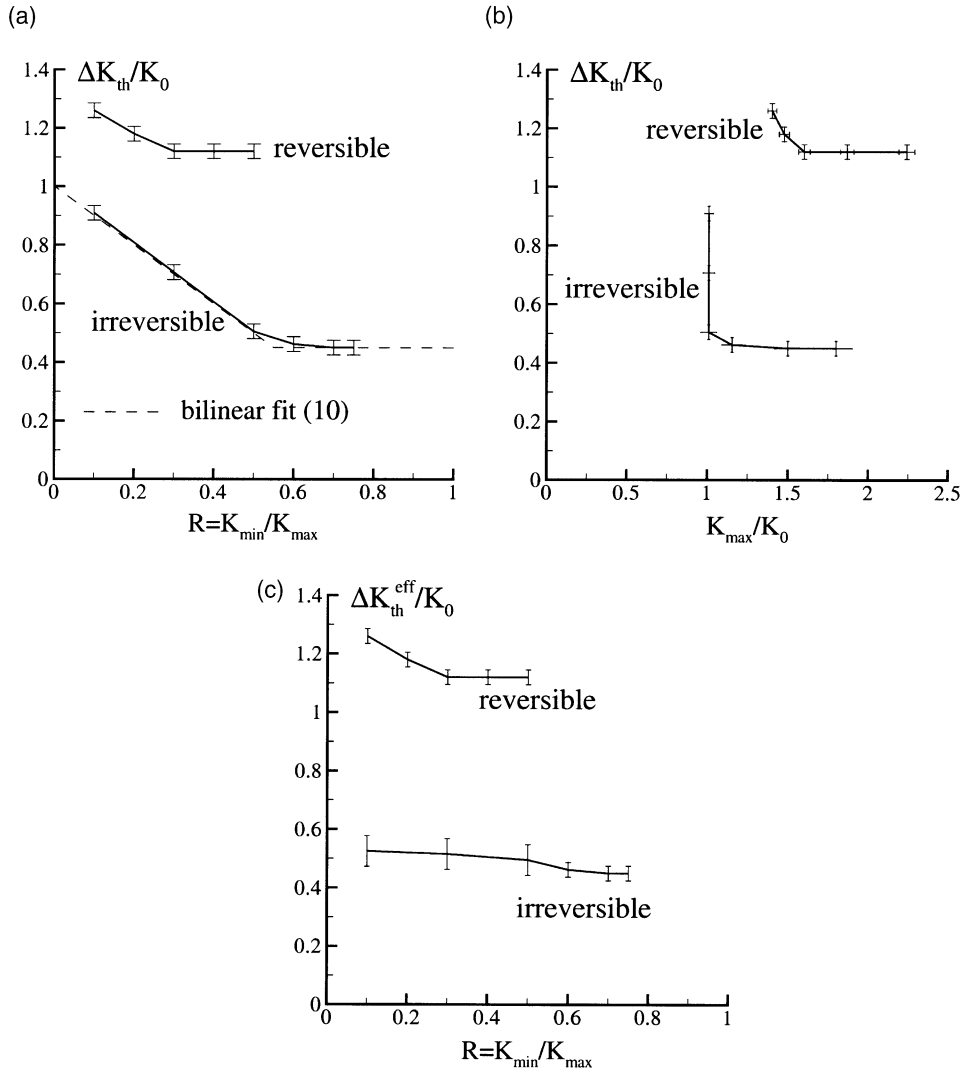
(a)

(b)

(c)

Fig. 5. (a) Variation of ΔK_{th} with load ratio R. (b) ΔK_{th} as a function of the applied K_{max}. (c) Load ratio dependence of the *effective* fatigue threshold ΔK_{th}^{eff}. The effective ΔK_I is defined through Equation (9). Note that the bars represent bounds on the appropriate quantities due to the fact that we have estimated ΔK_{th} by reducing the applied ΔK_I in discrete steps of $0.05K_0$.

location of the crack when $K_I = K_{op}$. Continued loading results in the contact zone retracting towards the original location of the crack tip until finally the crack completely opens. To quantify closure, we define d to be the distance from the current crack tip to the location where closure has occurred. Thus, $d/\Delta a = 1$ and 0 correspond to fully open and closed cracks, respectively. Curves of K_I/K_{max} versus $d/\Delta a$ are plotted in Fig. 7 for near-threshold values of ΔK_I (K_I is normalized by K_{max} to enable us to clearly plot all the curves in a single figure). After the first three or four cycles these curves settle down and do not change appreciably from cycle to cycle. Thus, for clarity only one loading and unloading cycle is shown in each case. We observe that:

1. Complete crack closure occurs for $R = 0.1, 0.3$ and 0.6 but not for $R = 0.7$.

2. The crack closure stress intensity factor, K_{cl}, and the crack opening stress intensity factor, K_{op}, are approximately equal and insensitive to the value of R. Upon noting that $K_{max}/K_0 \approx 1$ for the cases where closure occurred, we see that $K_{cl} \approx K_{op} \approx 0.5K_0$. This observation does not hold for ΔK_I values well above the fatigue threshold and it will be shown subsequently that for a fixed value of R, K_{cl} decreases with increasing ΔK_I.

3. The K_I/K_{max} versus $d/\Delta a$ curves flatten out as K_I approaches its peak value. The spurt of crack growth and ensuing fluctuations seen at the end of every loading cycle (see the inset in Fig. 6a) occur during this period.

We now proceed to examine the load ratio dependence of ΔK_{th} using the above closure observations. When the crack faces are in contact, the stresses in the
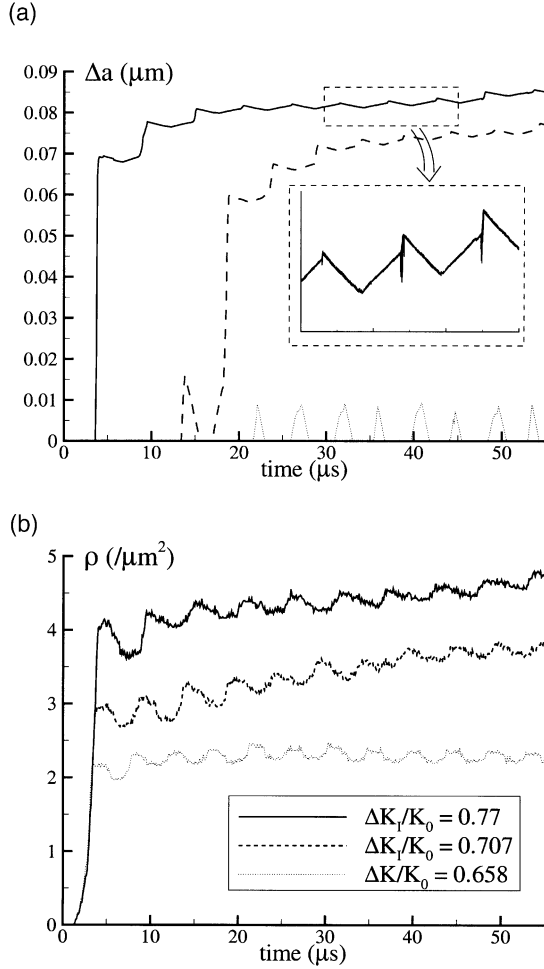
(a)

(b)

Fig. 6. (a) Time evolution of the crack growth and (b) time evolution of the dislocation density for the case with the irreversible cohesive surface law ($R = 0.3$).
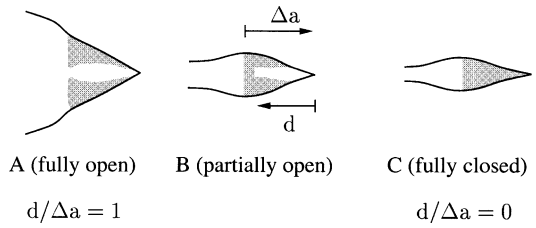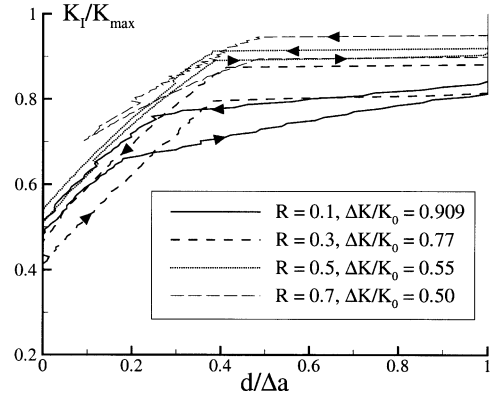

Fig. 7. The applied K_I versus crack closure for the case with the irreversible cohesive law and near-threshold values of ΔK_I. Crack closure is parameterized by $d/\Delta a$ with $d/\Delta a = 1$ and 0 corresponding to fully open and closed cracks, respectively. Only a single loading unloading cycle is shown in each case for the sake of clarity.

vicinity of the crack tip are much reduced, inhibiting dislocation nucleation and glide as well as lessening the driving force for separation. As a consequence, crack propagation generally takes place only during the fraction of the fatigue loading cycle in which the crack faces at the tip are separated, see, for example, Refs. [29, 30]. The effective stress intensity range ΔK^{eff} responsible for crack growth is:

$$\Delta K^{eff} = \begin{cases} K_{max} - K_{op} & \text{for } K_{min} < K_{op} \\ \Delta K_I & \text{for } K_{min} \geq K_{op}. \end{cases} \qquad (9)$$

Curves of ΔK_{th}^{eff} are plotted in Fig. 5c as a function of R. The absence of any load ratio effect for the irreversible cohesive law (as compared to that seen in Fig. 5a) suggests that the increase in ΔK_{th} with decreasing R is in fact a closure phenomenon; the

fatigue threshold with the irreversible cohesive law is at a constant *effective* threshold stress intensity factor range ΔK_{th}^*. Using the observation that the crack closure stress intensity factor $K_{cl} = K_{op}$ is approximately independent of R at threshold (Fig. 7), we rationalize the two distinct regions in the ΔK_{th} versus R plot as follows. For $K_{min} < K_{op}$ crack closure occurs and

$$\Delta K_{th} = (1 - R)(\Delta K_{th}^* + K_{op}) \qquad (10a)$$

where we have employed the relation $\Delta K = (1 - R)K_{max}$. No crack closure occurs for $K_{min} \geq K_{op}$ and the threshold criteria is simply given by

$$\Delta K_{th} = \Delta K_{th}^*. \qquad (10b)$$

Equation (10a) is equivalent to K_{max} at threshold having the constant value $\Delta K_{th}^* + K_{op}$ and equations (10a) and (10b) together imply that the transition in the ΔK_{th} versus R plot occurs at $R_c = K_{op}/(\Delta K_{th}^* + K_{op})$. Note that equation (10) has the same form as the Schmidt and Paris [31] model for the load ratio dependence of the fatigue threshold. However, the mechanism is different: K_{cl} in our plane strain calculations with the irreversible cohesive law is an outcome of surface contact due to the formation of oxide layers on newly created surfaces while Schmidt and

Paris [31] based their model on plasticity induced closure which is a plane stress phenomenon. Equation (10) with $\Delta K_{th}^* = 0.45K_0$ and $K_{op}/K_0 = 0.55$ is plotted in Fig. 5a and agrees very well with the numerical results. That $K_{op} + \Delta K_{th}^* \approx K_0$ for this reference case calculation is merely coincidental and it will be shown in Section that this does not generally hold. We emphasize that although $K_{max} \geq K_0$, which is a measure of the energy required to create the new crack surface, crack growth occurs under cyclic loading with K_{max} much less than the K_I value needed for the same crack to grow under monotonic loading conditions.

It is worth mentioning that, consistent with experiment as summarized in Ref. [2], our simulations show that ΔK_{th}^* for the irreversible cohesive surface is less than half the value for the reversible cohesive surface. Moreover, the "intrinsic" K_{max}^* does not play a role with the irreversible cohesive surface.

3.2. Parameter sensitivity

We now present three case studies with the aims of: (i) illustrating the sensitivity of the above results to material parameters; and (ii) assessing the ability of the model to capture certain well-known experimental observations related to fatigue crack growth.

3.2.1. Effect of obstacle density. The irreversibility of dislocation motion was seen to be the origin of continued crack growth under cyclic loading. Since pinning of dislocations at obstacles has a major effect on this irreversibility, we present results for a material with a lower obstacle density of $\rho_{obs} = 145/\mu m^2$ but otherwise identical to the reference case with the irreversible cohesive law.

A comparison between the monotonic crack growth resistance curves of the reference case and a low obstacle density material is shown in Fig. 8a. Crack growth in the low obstacle density material initiates at a higher value of $K_I/K_0 \approx 1.24$. Subsequently, there is an increase in the resistance to crack growth and the *R*-curves of the two materials converge for $\Delta a > 0.2\ \mu m$. Under cyclic loading conditions, the crack growth behavior of the low obstacle density material was found to be qualitatively similar to that of the reference material and here we only summarize the results for ΔK_{th}.

The ΔK_{th} versus R plot for the low obstacle density material is shown in Fig. 8b. Again we see that ΔK_{th} decreases approximately linearly with R and then plateaus out at $R_c \approx 0.7$. An analysis similar to that described above revealed that this value of R corresponded to the onset of crack closure: complete crack closure occurred in this case at $K_{cl} \approx 0.8K_0$. Thus, in line with our findings for the reference case, the two regions in the ΔK_{th} versus R plot emerge due to crack closure and the bilinear relation (10) fits the numerical results rather well with $K_{op}/K_0 = 0.79$ and $\Delta K_{th}^*/K_0 = 0.39$.

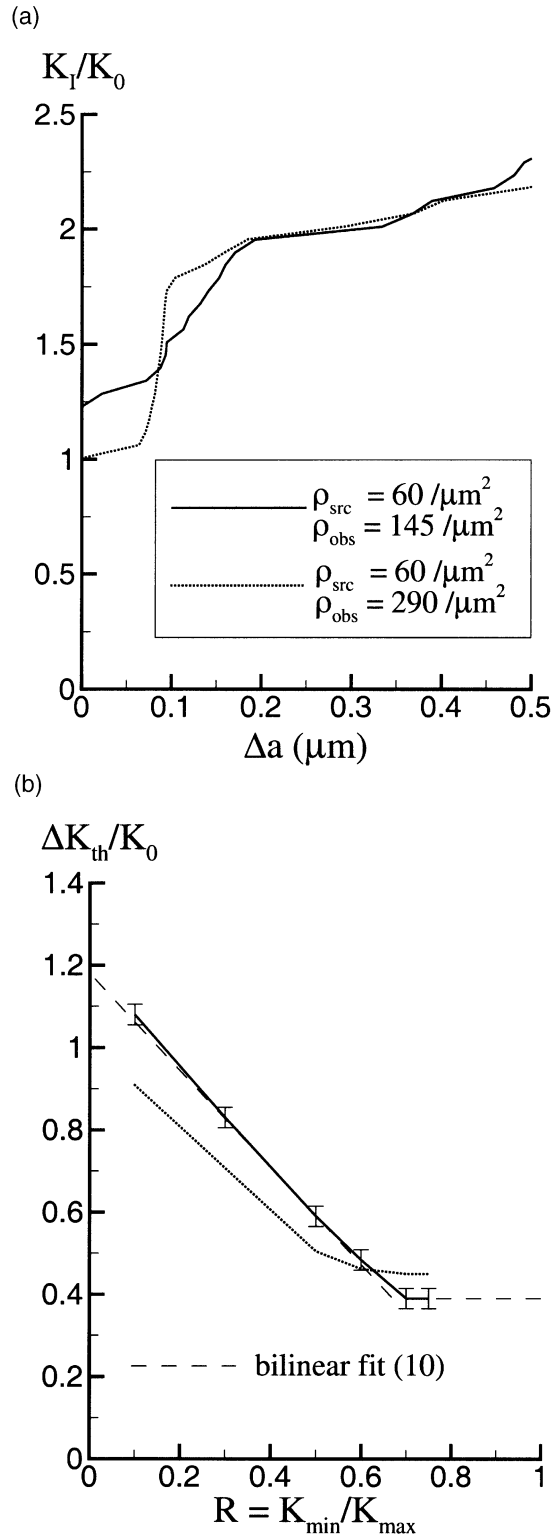A comparison between the fatigue threshold values, ΔK_{th}, for the reference and low obstacle den-

(a)

(b)

Fig. 8. (a) Applied stress intensity factor K_I/K_0 versus crack extension Δa for two obstacle densities. The source density is $\rho_{src} = 60/\mu m^2$. (b) Fatigue threshold as a function of the load ratio for the two obstacle densities considered. Note that the bars represent bounds on ΔK_{th} due to the fact that we have estimated ΔK_{th} by reducing the applied ΔK_I in discrete steps of $0.05K_0$.

sity materials is also shown in Fig. 8b. Corresponding to the 20% higher monotonic crack growth initiation stress intensity factor, ΔK_{th} for the low obstacle density material is also about 20% higher than that of the reference material at low values of R. However, this trend reverses for higher R values with ΔK_{th}^* for the low obstacle density material being lower than that for the reference case material. This can be understood by noting that when the obstacle density is lowered, there are fewer dislocations piled up at obstacles. Hence, in the high R regime where the dislocation density is high, lowering the obstacle density acts to increase the mobility of dislocations which means a smaller ΔK_I is needed to induce dislocation motion during the unloading–reloading part of the cycle. Thus, ΔK_{th}^* is indeed expected to decrease with decreasing obstacle density. On the other hand, for low values of R, ΔK_{th} is dominated by crack closure. In these simulations the reduced obstacle density increased K_{op} which resulted in an increase in ΔK_{th}.

Cyclic loading simulations with the reversible cohesive law indicated that the fatigue thresholds of the low obstacle density material are very high, for example, for $R = 0.3$, $\Delta K_{th}/K_0 > 1.7$. The high ΔK_I values (with correspondingly high dislocation densities) made the computations extremely time consuming and therefore detailed results for this case are not presented. Nevertheless, the calculations indicate that with the reversible cohesive law the fatigue threshold values for the low obstacle density material are substantially higher than the corresponding values for the high obstacle density, reference material. This contrasts with the fatigue thresholds for the low obstacle density and high obstacle density materials differing by only about 20% when the irreversible cohesive law is employed.

3.2.2. Effect of tensile overloads. The Paris law which is commonly used to quantify crack growth rates at post-threshold ΔK_I values breaks down when the crack is subjected to a sudden tensile overload [32]. In particular, a single tensile overload may significantly retard crack growth. Here we carry out calculations in the post-threshold regime and investigate the predictions of the present model regarding this well-documented overload effect. While in experiments the overload is typically applied after nominally steady state conditions have been attained, for computational reasons we apply the overload in the second cycle. The reference material parameters with the irreversible cohesive surface are used.

First, consider constant amplitude loading with $R = 0.3$ and $\Delta K_I/K_0 = 0.90$ as shown in Fig. 9a. From the time evolution of the crack growth plotted in Fig. 9b we see that the crack growth is accelerating for the first seven cycles. The calculations were stopped after the crack had advanced by about 0.20 μm as dislocations by then are approaching the boundary of the process window. Some insights into the mechanisms of crack growth at this higher applied ΔK_I are

gained by examining the time evolution of the crack closure parameter $d/\Delta a$ shown in Fig. 9c. Crack closure with $d/\Delta a = 0$ occurs for the first six cycles and then a state with no crack closure is achieved. This indicates that $\Delta K_I/K_0 = 0.90$ corresponds to a Stage II stress intensity factor range; no crack closure even at low R values is characteristic of Stage II crack growth [1]. Examination of the results reveals that K_{cl} is reducing during the first six cycles and then settles down to a value less than $K_{min} = 0.39K_0$, thus precluding crack closure. For this high value of $\Delta K_I/K_0 = 0.90$, K_{cl} has a "steady-state" value less than the value $0.5K_0$ seen under near-threshold conditions. This post-threshold loading case clearly illustrates continued crack growth under cyclic loading conditions at a value of K_{max} at which the crack would have arrested under monotonic loading: with $K_{max}/K_0 \approx 1.29$, the crack grows by about 0.2 μm after eight cycles (Fig. 9b), whereas $K_I/K_0 \approx 2.0$ is needed for the crack to grow by that length under monotonic loading conditions (Fig. 9b).

Next consider two loading histories with a single tensile overload on the second loading cycle but otherwise identical to the constant amplitude loading case considered above:

1. a single overload 8% above the nominal K_{max}: The overload cycle causes an additional crack advance of about 0.005 μm followed by retarded crack growth; after 10 cycles the overloaded crack advanced $\Delta a \approx 0.1$ μm as compared to $\Delta a \approx 0.22$ μm in the constant amplitude loading case. This retardation can be understood by observing that crack closure continues beyond the sixth cycle (Fig. 9c). Thus, the effective driving force on the crack is lower than that in the constant amplitude loading case so that the crack growth rate is reduced. This calculation was continued for 15 cycles, but typically the retarded growth rates are seen for >200 post-overload cycles [32], which is much larger than the number of cycles computationally feasible here.
2. a single overload 16% above the nominal K_{max}: The overload results in an additional crack advance of about 0.05 μm. Subsequently, da/dN approximately equal to that for the constant K_{max} case is prematurely attained as the overload hastens the end of crack closure.

3.2.3. Effect of slip geometry. In the near-threshold region, plastic zone sizes are small and the discreteness of the dislocation fields is expected to play an important role in governing the crack growth behavior. In the two-dimensional analysis presented above, the material had three slip systems, so that there is a redundancy in available slip systems, as for three-dimensional fcc and bcc crystals. Now consider a crystal identical to the reference material but with the $\phi^{(\alpha)} = 0°$ slip planes deactivated. With a slip system flow strength τ_o, an asymptotic analysis [33] for
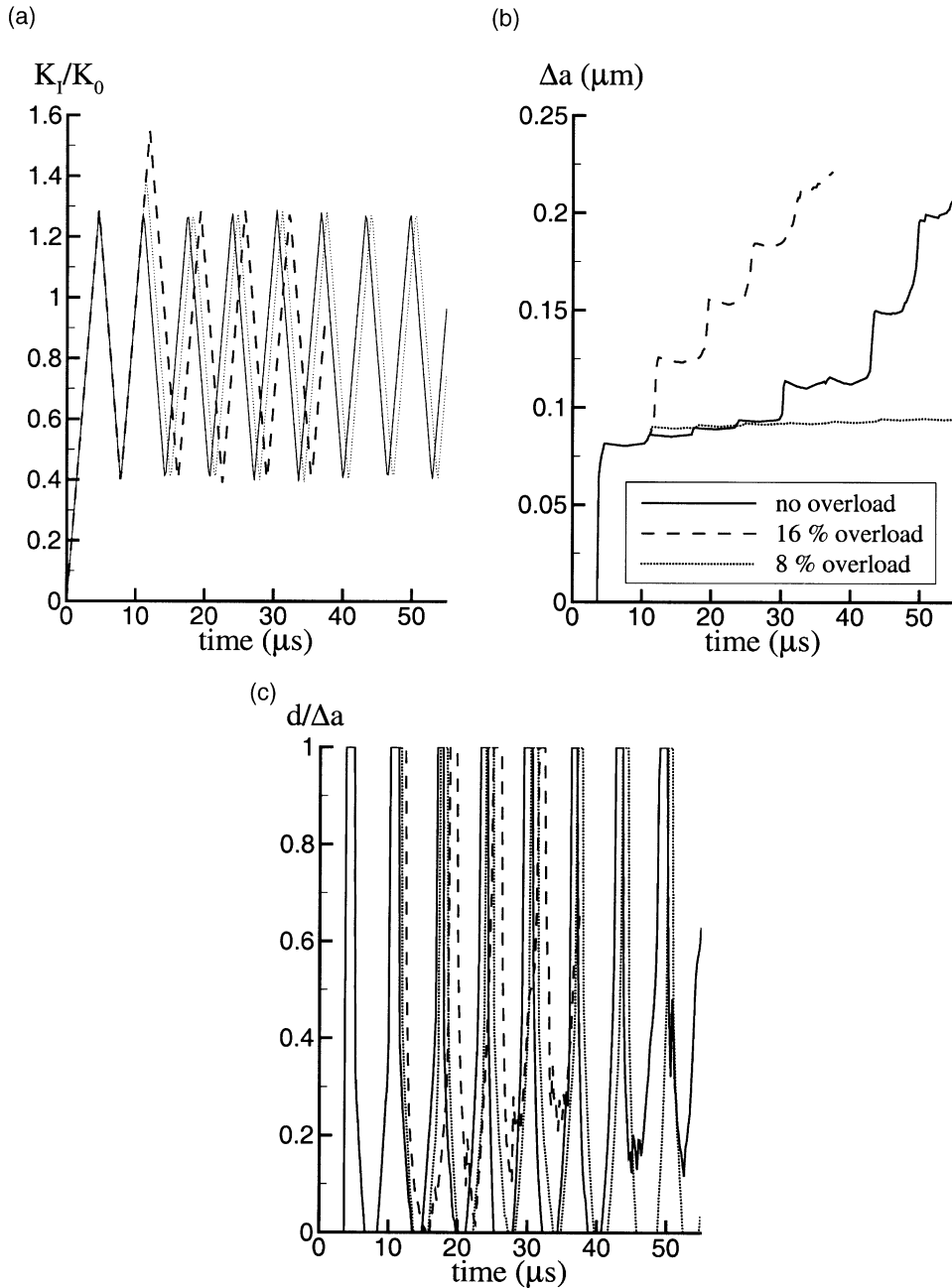
(a)

(b)

(c)

Fig. 9. (a) The applied stress intensity factor as a function of time with $R = 0.3$ and (i) no overload with $\Delta K_I/K_0 = 0.90$; (ii) 8% overload on the second cycle; (iii) 16% overload on the second cycle. (b) Evolution of the crack advance with time for these three cases. (c) Crack closure as parameterized by $d/\Delta a$ for three loading histories shown in (a).

a stationary crack under monotonic loading conditions, predicts that the crack opening stresses for the two and three slip system materials are $4\sqrt{3}\tau_o \approx 6.93\tau_o$ and $10\tau_o/\sqrt{3} \approx 5.77\tau_o$, respectively. Thus, continuum crystal plasticity predicts that the three slip system material is more effective in relaxing the near-tip stresses and hence would be expected to have a higher resistance to crack growth. It is worth mentioning here that away from the near-tip region the stress levels in the discrete dislocation

simulations of Van der Giessen *et al.* [12] agree very well with the continuum plasticity values.

Discrete dislocation predictions (with the irreversible cohesive law) of monotonic crack growth resistance curves for the two and three slip system materials are shown in Fig. 10a. The remote applied K_I required to propagate a crack in the two slip system material is about 20% higher than that required for the three slip system material. Next consider cyclic crack growth. The discrete dislocation predictions
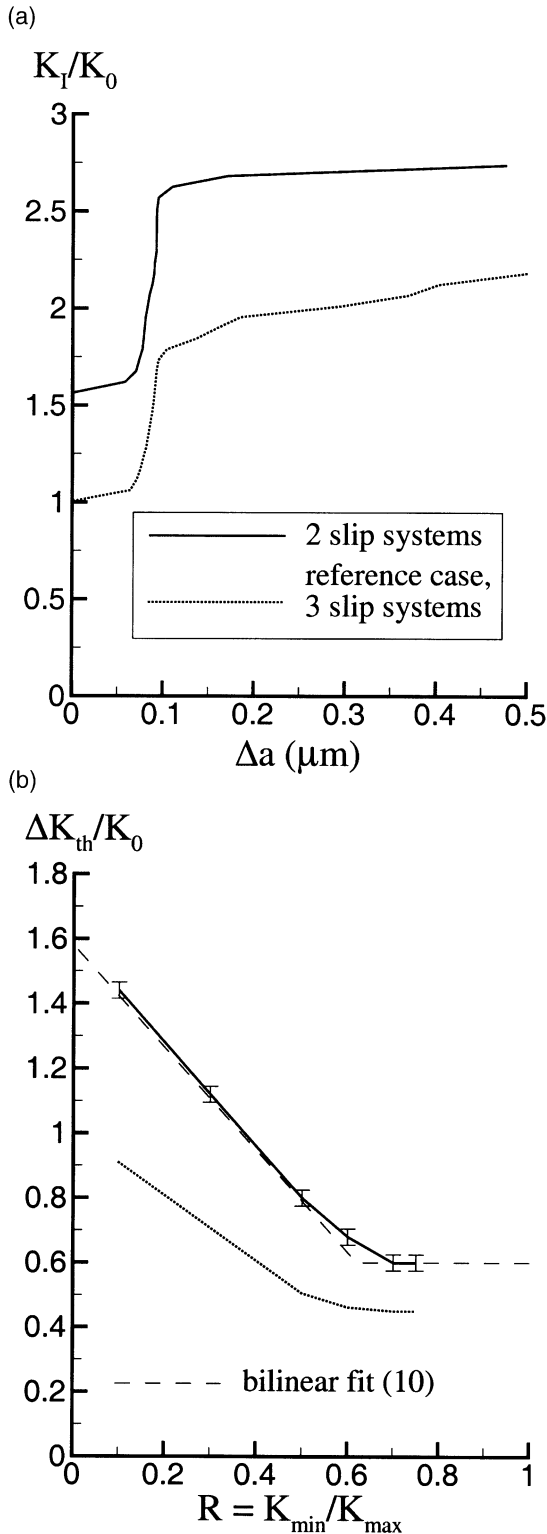
(a)

(b)

Fig. 10. (a) Comparison between the applied stress intensity factor K_I/K_0 versus crack extension Δa for a material with two slip systems and for the reference material. (b) Fatigue threshold as a function of the load ratio for the reference case and two slip system materials. Note that the bars represent bounds on ΔK_{th} due to the fact that we have estimated ΔK_{th} by reducing the applied ΔK_I in discrete steps of $0.05K_0$.

of the near-threshold fatigue crack growth behavior were qualitatively similar for the two and three slip system materials with crack closure occurring in both cases at low R values. A comparison between ΔK_{th} for the materials is shown in Fig. 10b: the fatigue threshold of the two slip system material is at least 20% higher than that of the three slip system material for all values of R considered. Thus, contrary to expectations based on conventional continuum crystal plasticity, the monotonic and cyclic crack growth resistance of the two slip system material is higher than that of the three slip system material. These results indicate that the dislocations on the slip systems parallel to the crack do not relax the near tip stresses but have an anti-shielding effect. However, analytical expressions for the stress fields due to edge dislocations around the tip of a semi-infinite sharp crack [34] show that dislocations on slip planes parallel to the crack do not in fact contribute to the mode I stress intensity factor. This suggests that the anti-shielding results from the different dislocation structures that develop on the inclined slip planes due to the presence of dislocations on the 0° slip planes.

4. DISCUSSION

In the models of Pippan and co-workers [4–6] and Wilkinson *et al.* [7], dislocation nucleation is assumed to occur exclusively from the crack tip (or a single source near the crack tip) and crack growth is taken to occur when a specified slip criterion is met, which does not require high stresses at the crack tip. These models do not address crack growth behavior under monotonic loading conditions. Also, any contribution of dislocations nucleated away from the immediate crack tip region to the local stress field or to the plastic dissipation is neglected. By way of contrast, crack growth by material separation, which requires high crack tip stresses, is a direct outcome of our calculations under both monotonic and cyclic loading conditions. The fracture and plasticity characteristics of the material are specified independently and, in particular, the same discrete dislocation parameters are used to characterize plastic flow when there is no initial crack (e.g. in bending [10]).

Our simulations exhibit several features that are in remarkable accord with what is seen experimentally. In addition, the simulations make predictions about aspects of fatigue crack growth that have not yet been conclusively resolved experimentally. For example, it has been suggested [2] that current experimental methods may overestimate the reduction in the effective ΔK caused by crack closure and that the $R = K_{min}/K_{max}$ dependence of the fatigue threshold cannot be solely attributed to premature closure of the crack. The calculations modeling both perfect vacuum and oxidizing environmental conditions exhibit a dependence of the fatigue threshold on R. With a reversible cohesive law this is an outcome of insufficient plasticity at low R values whereas with an irre-

versible cohesive law, the R dependence is an outcome of crack closure at low values of R. For both cohesive laws, we find the fatigue threshold to be insensitive to R for larger values of R. Also, various mechanisms for crack growth retardation following a tensile overload have been proposed (e.g. crack tip blunting, an enlarged zone of residual compressive stresses, activation of near-threshold mechanisms, see Ref. [1]). In our calculations a small overload enhances crack closure which results in a retardation in the crack growth rate.

Vasudevan *et al.* [2] analyzed fatigue threshold data from the literature and rather surprisingly observed that irrespective of material composition, crystallographic structure etc. the values of $\Delta K_{th}^*/K_{max}^*$ for materials tested in vacuum and air were about 1.0 and 0.4, respectively. This is in good agreement with our results: we obtain $\Delta K_{th}^*/K_{max}^* \approx 0.8$ for the reference case material with the reversible cohesive law and $\Delta K_{th}^*/K_{max}^* \approx 0.4$, 0.33 and 0.38 for the reference, high obstacle density and two slip system materials, respectively, with the irreversible cohesive law. However, the absolute values of ΔK_{th} obtained from our simulations are much lower than seen experimentally. With $K_0 = 0.358$ MPa$\sqrt{m}$, our calculations predict $\Delta K_{th}^* \approx 0.4$ MPa$\sqrt{m}$ in vacuum and $\Delta K_{th}^* \approx 0.16$ MPa$\sqrt{m}$ in air. These are nearly an order of magnitude lower than the corresponding values for Al alloys reported in Ref. [2]. The discrepancy may be due to several idealizations in the model. For example, for numerical reasons, we have used a value of K_0 that is about a factor of 2 smaller than representative of aluminum and the amount of plastic dissipation accompanying crack growth will increase with increasing cohesive strength; a high loading rate is used to reduce the computing time and this also acts to decrease the amount of plastic dissipation; the analyses are carried out for pure mode I loading with symmetry assumed about the crack plane, while in single crystals mixed mode loading conditions generally prevail at the crack tip [35]; the model is purely two dimensional, with both three-dimensional dislocation effects and three-dimensional crack growth effects neglected; and the effects of crack tip blunting are not taken into account in our small strain analyses. However, it is also possible that at least some of the discrepancy arises because the calculations are carried out for small amounts of straight ahead crack growth in a single crystal, while experimental values typically pertain to much larger amounts of crack growth in a polycrystal, with effects such as crack growth off the initial crack plane and interactions with grain boundaries possibly coming into play.

It is important to note that both the discrete dislocation framework and the cohesive surface framework are extensible. Each applies in a broad range of circumstances beyond crack growth under cyclic loading conditions. The formulation used here can be extended, for example, to mixed mode loading conditions, to allow crack growth off the initial crack

plane and to fully account for three-dimensional effects, albeit at a greatly increased computational cost. Of particular interest is extending the computations into the post-threshold regime to explore whether or not a Paris-type law for crack growth emerges from our formulation and, if it does, what its dependence is on various parameters.

5. CONCLUSIONS

Analyses of near-threshold fatigue crack growth in model single crystals under mode I plane strain conditions have been carried out where plastic flow arises from the collective motion of large numbers of discrete dislocations and the fracture properties are embedded in a cohesive surface constitutive relation. The only difference between the boundary problem formulations for monotonic and cyclic loading is the prescribed time variation of the remote stress intensity factor. Cohesive constitutive relations representing reversible separation, as may occur in a perfect vacuum, and irreversible separation, as in an oxidizing environment have been employed. General features that emerge from the calculations include:

- Crack growth occurs under cyclic loading conditions when the driving force is smaller than what is needed for the crack to grow under monotonic loading conditions.
- The origin of continued crack growth under cyclic loading lies in the irreversibility of dislocation motion.
- Under cyclic loading conditions as well as under monotonic loading conditions, the crack advances due to locally high stress concentrations ahead of the crack mediated by clustering of dislocations near the tip. Because of this, the relative fracture resistances of three slip system and two slip system crystals is the opposite of what would be expected based on conventional continuum plasticity.
- The predicted fatigue crack growth threshold depends sensitively on the irreversibility of the cohesive surface. For a reversible cohesive surface, the occurrence of fatigue is controlled entirely by the irreversibility of dislocation motion. For an irreversible cohesive surface, crack closure plays a key role in setting the fatigue threshold with ΔK_{th}^{eff} being nearly insensitive to the value of the loading ratio $R = K_{min}/K_{max}$ (see Fig. 5c).
- In the post-threshold regime, a sufficiently small overload is found to retard crack growth while a larger overload is found to accelerate crack growth. The mechanism for this is that the small overload promotes crack closure while the larger overload hastens the end of crack closure.
- The predictions for the qualitative features of the fatigue crack growth threshold, such as the form of its dependence on the loading ratio R, are in

remarkable accord with experimental observations.

REFERENCES

1. Suresh, S., *Fatigue of Materials*. Cambridge University Press, Cambridge, UK, 1991.
2. Vasudevan, A. K., Sadananda, K. and Louat, N., *Mater. Sci. Engng A*, 1994, **188**, 1.
3. Riemelmoser, F. O., Gumbsch, P. and Pippan, R., *Mater. Trans.*, 2001, **42**, 2.
4. Pippan, R., *Acta Mat.*, 1991, **39**, 255.
5. Riemelmoser, F. O. and Pippan, R., *Mater. Sci. Engng A*, 1997, **234-236**, 135.
6. Riemelmoser, F. O., Pippan, R. and Stüwe, H. P., *Int. J. Fract.*, 1997, **85**, 157.
7. Wilkinson, A. J., Roberts, S. G. and Hirsch, P. B., *Acta mater.*, 1998, **46**, 379.
8. Laird, C. and Smith, G. C., *Phil. Mag.*, 1962, **7**, 847.
9. Neumann, P., *Acta metall.*, 1969, **17**, 1219.
10. Cleveringa, H. H. M., Van der Giessen, E. and Needleman, A., *Int. J. Plast.*, 1999, **15**, 837.
11. Cleveringa, H. H. M., Van der Giessen, E. and Needleman, A., *J. Mech. Phys. Solids*, 2000, **48**, 1133.
12. Van der Giessen, E., Deshpande, V. S., Cleveringa, H. H. M. and Needleman, A., *J. Mech. Phys. Solids*, 2001 (in press).
13. Van der Giessen, E. and Needleman, A., *Modeling Simul. Mater. Sci. Engng*, 1995, **3**, 689.
14. Kubin, L. P., Canova, G., Condat, M., Devincre, B., Pontikis, V. and Bréchet, Y., *Solid State Phenom.*, 1992, **23**, 455.
15. Needleman, A., *J. Appl. Mech.*, 1987, **54**, 525.
16. Harding, T. S. and Wayne Jones, J., *Metall. Mat. Trans.*, 2000, **31A**, 1741.
17. Dubey, S., Soboyejo, A. B. O. and Soboyejo, W. O., *Acta mater.*, 1997, **45**, 2777.
18. Mercer, C., Soboyejo, A. B. O. and Soboyejo, W. O., *Acta mater.*, 1999, **47**, 2727.
19. Needleman, A., *J. Mech. Phys. Solids*, 1990, **38**, 289.
20. Freund, L. B., *Adv. Appl. Mech.*, 1990, **30**, 1.
21. Rose, J. H., Ferrante, J. and Smith, J. R., *Phys. Rev. Lett.*, 1981, **47**, 675.
22. Pelloux, R. M. N., *Trans. Am. Soc. Met.*, 1969, **62**, 281.
23. Pelloux, R. M. N., *Eng. Frac. Mech.*, 1970, **1**, 697.
24. de-Andrés, A., Pérez, J. L. and Ortiz, M., *Int. J. Solids Struct.*, 1999, **36**, 2231.
25. Nguyen, O., Repetto, A., Ortiz, M. and Radovitzky, R. A., *Int. J. Fract.*, 2001, **110**, 351.
26. Rice, J. R., *J. Appl. Mech.*, 1968, **35**, 379.
27. Morrissey, J. W. and Rice, J. R., *J. Mech. Phys. Solids*, 1998, **46**, 467.
28. Cleveringa, H. H. M., Van der Giessen, E. and Needleman, A., *Mater. Sci. Engng* 2001 (in press).
29. Elber, W., *Engng Fract. Mech.*, 1970, **2**, 37.
30. Budiansky, B. and Hutchinson, J. W., *J. Appl. Mech.*, 1978, **45**, 267.
31. Schmidt, R. A. and Paris, P. C., *ASTM STP*, 1973, **536**, 79.
32. Elber, W., *ASTM STP*, 1971, **486**, 230.
33. Rice, J. R., *Mech. Mater.*, 1987, **6**, 317.
34. Lakshmanan, V. and Li, J. C. M., *Mater. Sci. Engng*, 1988, **A104**, 95.
35. Chan, K. S., Hack, J. E. and Leverant, G. R., *Metall. Trans.*, 1987, **18A**, 581.